IEEE Photonics Journal
An IEEE Photonics Society Publication

Invited Paper

High-Speed Buried Tunnel Junction Vertical-Cavity Surface-Emitting Lasers

Volume 2, Number 5, October 2010

Werner Hofmann, Member, IEEE

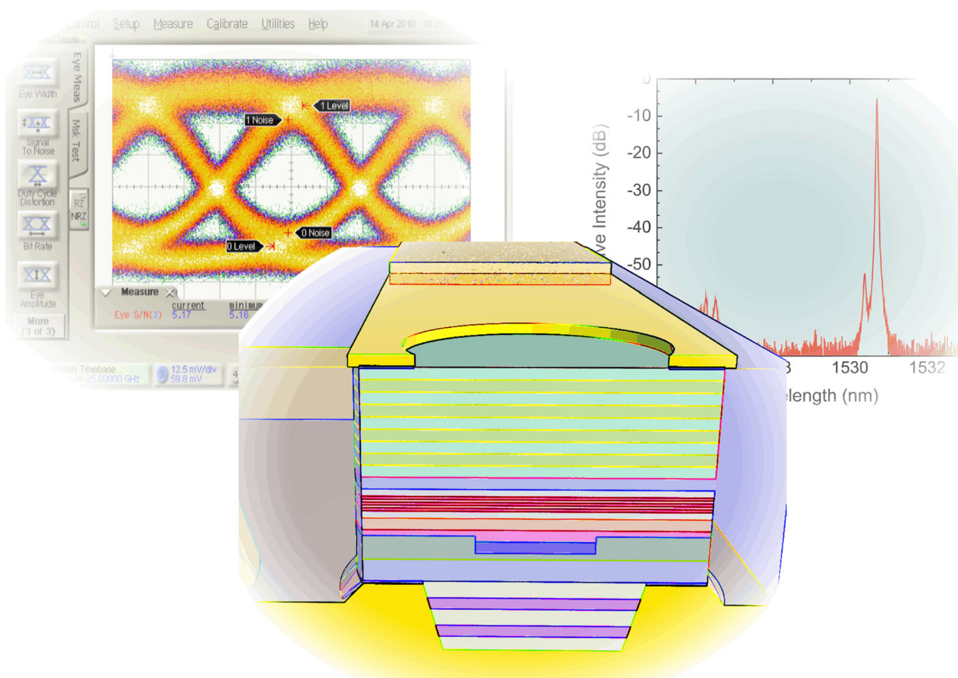

DOI: 10.1109/JPHOT.2010.2055554
1943-0655/$26.00 ©2010 IEEE

IEEE photonics SOCIETY

IEEE

High-Speed Buried Tunnel Junction Vertical-Cavity Surface-Emitting Lasers

Werner Hofmann, ***Member, IEEE***

(Invited Paper)

Walter Schottky Institute, Technical University of Munich, 85748 Garching, Germany
Department of Electrical Engineering and Computer Science, University of California at Berkeley, Berkeley, CA 94720 USA
Institute of Solid State Physics, Technical University of Berlin, 10623 Berlin, Germany

DOI: 10.1109/JPHOT.2010.2055554
1943-0655/$26.00 ©2010 IEEE

Manuscript received April 29, 2010; revised June 21, 2010; accepted June 22, 2010. Date of publication June 28, 2010; date of current version September 10, 2010. This work was supported by the German Academic Exchange Service (DAAD) through a fellowship at the University of California at Berkeley within the Postdoc-Program, the National Science Foundation through CIAN under Grant EEC-0812072, and the German Research Council (DFG) for funding via SFB 787. Corresponding author: W. Hofmann (e-mail: Werner.Hofmann@tu-berlin.de).

Abstract: InP-based, vertical-cavity surface-emitting lasers (VCSELs) utilizing a buried tunnel junction (BTJ) emitting at 1.55 μm with improved active region and reduced parasitics are demonstrated. A superior modulation bandwidth $>$ 10 GHz is achieved up to 85 °C. The VCSEL device is investigated in detail, analyzing all bandwidth-limiting elements. With their improved temperature range, these VCSELs are especially qualified for uncooled operation in passive optical networks. These lasers show open eyes and error-free transmission up to 25-Gb/s modulation speed at room temperature. Uncooled error-free operation over a wide temperature range under constant bias conditions for ultra-low-cost systems is demonstrated at a 12.5-Gb/s data rate up to 85 °C. Due to a well-tailored mode-gain detuning, the laser characteristics are practically invariant with temperature at fixed bias conditions. Further possible design optimizations targeting at data rates well above 25 Gb/s are discussed.

Index Terms: Vertical-cavity surface-emitting laser (VCSEL), high-speed modulation.

1. Introduction

The first vertical-cavity surface-emitting laser (VCSEL) was proposed more than 30 years ago [1], and devices with internal bandwidths exceeding 20 GHz have been presented recently, emitting in the near-infrared spectrum [2], [3]. As this waveband can only be used for short distances up to 300 m, there has been a great effort in developing long-wavelength, high-speed VCSELs with steady progress [2]–[8]. In the long-wavelength regime around 1.3 and 1.55 μm, devices with satisfying performance were demonstrated only over the past decade [4]–[11]. The main challenge, compared with VCSELs grown on GaAs substrate, which we can find nowadays in each laser-mouse for the personal computer, are the poor epitaxial distributed Bragg reflectors (DBRs) lattice matched on InP, which are the substrate of choice for an active region for long-wavelength VCSEL devices. Incorporating ternary and quaternary alloys, these mirrors have one order of magnitude worse thermal conductivity than the GaAs-Al(Ga)As DBR stacks for short-wavelength devices. Furthermore, the refractive index contrast is low. This translates, together with the longer wavelengths, into

very thick mirrors with large photon penetration depths, making devices incorporating *p*-doped epi-mirrors with large electrical and optical losses extremely difficult to realize.

On the other hand, VCSELs are preferred light sources in many fields because of their low cost and advanced packaging capability, single longitudinal mode operation with narrow circular beam for direct fiber coupling, 1-D and 2-D arrays defined by lithography, high-speed modulation at low driving currents and last, but not least, low power consumption, reducing the whole system cost with smaller electrical driver circuits, boards, form-factors, power-budgets and cooling racks. Especially for green-IT, VCSELs are a promising environmentally friendly solution, conserving system power and cost. In the near future, the market will demand cost-effective 100G Ethernet solutions. Consequently, higher laser bandwidth is demanded for the projected data rates, favorably provided by a cost-effective device at long wavelengths and high temperatures that range up to 85 °C for uncooled operation.

Most technical approaches successfully realizing long-wavelength VCSELs for the optical communications wavelengths introduced a tunnel-junction to get rid of the *p*-doped epi-mirror in order to lower the cavity losses [4]–[9]. Also, dielectric top DBRs have been used, replacing inefficient mirrors from semiconductor material. A quite promising approach for high-speed applications utilizes a buried tunnel junction (BTJ) as a current aperture converting *p*- into *n*-material, together with a buried hybrid reflector taking benefit of the material properties of gold with its high reflectivity in the infrared and its good thermal conductivity [9]. Another approach uses GaAs-based DBRs wafer-fused on an InP-based active region [5] or replacing both epi-mirrors with dielectric reflectors [8]. With these approaches, reliable devices and large-area VCSEL arrays [6], VCSELs with high output power at high temperatures [11], high data rates above 20 Gb/s [7], or modulation bandwidths in excess of 15 GHz [8] have been demonstrated recently. This review-article will summarize the works which originated at the Walter Schottky Institute, presenting high-speed long-wavelength BTJ VCSELs with superior bandwidths up to 85 °C.

This paper is organized as follows. The device layout is depicted in Section 2, and proprietary design concepts like the hybrid mirror or the BTJ are discussed. Speed-limiting elements are presented in Section 3, and an improved design is derived by equivalent circuit analysis. Device properties are given and discussed in Section 4, while further device concepts are presented in Section 5.

2. Long-Wavelength VCSEL High-Speed Design

The high-speed long-wavelength BTJ VCSEL presented here features a highly strained active region, optimized doping levels for reduced intrinsic parasitics, together with a low-parasitic chip layout. A BTJ, the dimensions of which are precisely controlled by lithography, serves as current aperture. Additionally, due to the BTJ, most of the *p*-conducting material with high electrical and optical losses is replaced by *n*-material. InP, which is a good thermal conductor, is used both at the *n*- and the *p*-side of the device, serving mutually as current and heat-spreader. The active region was tailored to emit at 1550 nm. The lasers under investigation were grown by molecular beam epitaxy on InP substrate. The high-speed 1.55-μm VCSEL structure is an improved version of the device described in [6], with optimized active region, detuning, mirror-reflectivities, and doping levels. The schematic layout of the laser chip is shown in Fig. 1.

Benzo-cyclo-butene (BCB), which is a silicate plastic, is used as low-dielectric constant passivation, eliminating contact pad capacitances. With this proprietary and substrate-less design, the whole laser chip consists of gold with dielectric passivation on top. This layout is more microstrip-like than being a coplanar electrical waveguide like most other high-speed VCSELs on semiconductor substrate. This electrical layout—with optimized pad design—is good for driving chips up to 100 GHz.

For high laser bandwidth and sufficient gain at elevated temperatures, the active region is composed of seven heavily strained (2.5% compressive strain, pseudomorphic) InAlGaAs quantum wells near the borderline of critical layer thickness. Highly strained active regions also showed superior bandwidth in 850-nm VCSELs [12]. For the presented device, the threshold current was

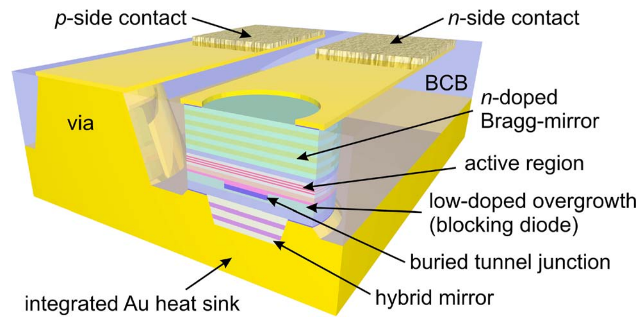

Fig. 1. Schematic cross-section of a high-speed 1.55-μm InP-based BTJ VCSEL. The device is mounted epi-down on an electroplated gold pseudosubstrate. The InP substrate is removed while manufacturing. Both *n*- and *p*-contact can be accessed on top. Contact-pad capacitances are minimized. A reduction of parasitic response was achieved by a low-doped layer in the overgrowth.

designed to be lowest at 60 °C heat-sink temperature. This was achieved by a large mode-gain offset, resulting in negative T_0 values. Due to the BTJ, which allows the elimination of nearly all *p*-conducting material with higher electrical resistances and optical losses, a differential series resistance as low as 40–50 Ω has been achieved and is impedance matched to electrical drivers.

As the parasitic response of these VCSELs can be well modeled by a first-order equivalent circuit [6], a three-pole filter function including relaxation-oscillation frequency f_R, intrinsic damping γ, and parasitic rolloff f_p describes the response of our VCSEL well, allowing several intrinsic parameters to be extracted. Constant terms in (1) are the differential quantum efficiencies η_d of laser and detector

$$H(f) = \eta_{d,L}\eta_{d,PD} \cdot \frac{f_R^2}{f_R^2 + j\frac{\gamma}{2\pi}f - f^2} \cdot \frac{1}{1 + j\frac{f}{f_P}}. \tag{1}$$

Even though our devices in reference design [6] showed excellent high-speed behavior for small chip diameters, the bandwidth of devices with larger semiconductor chips were still clearly limited by device parasitics. By reducing the doping levels of the blocking diode next to the BTJ from 5 to $1 \cdot 10^{17}$ cm^{-3}, the parasitic capacitance was significantly lowered, boosting the modulation bandwidth.

Furthermore, the hybrid backside mirror both features very high reflectivities larger than 99.95% and low penetration depths of the optical wave due to high refractive index contrast lossless material. The gold (or potentially silver) termination enables good thermal properties, together with compact mirrors of very high reflectivity. The device presented here has a quite proprietary if not exotic structure accommodating the physical challenges in the long wavelength regime. Therefore, the hybrid mirror and the BTJ shall be briefly discussed here.

2.1. Reflector Design

Epitaxially grown DBRs are not the mirror of choice for long-wavelength VCSELs. The hybrid mirror as back-reflector utilizing the high infrared reflectivity and thermal conductivity of gold at the same time is a very elegant solution for long-wavelength VCSELs. The high refractive index contrast pins the phase of the standing cavity wave and shortens photon lifetimes.

These hybrid mirrors can be very easily designed and evaluated for a certain Bragg wavelength. A DBR consists, as depicted in the upper part of Fig. 2, of an alternating sequence of high and low refractive index layers with a thickness of a quarter wavelength. The shown DBR, like that deployed in the reference VCSEL, is fabricated on top of a substrate with refractive index n_s, starting with a sequence of mirror pairs with refractive index n_1 and n_2. After N mirror-pairs, the mirror ends into a medium with n_r. We are interested in the amplitude and power reflectivities ρ and R for the Bragg wavelength at the center of the stop-band.

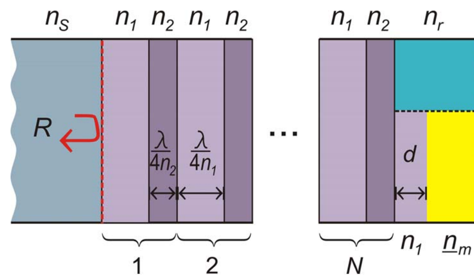

Fig. 2. Schematic hybrid Bragg reflector layout with N mirror pairs. Different from a classical Bragg reflector, which is given in the upper part of the schematic, this mirror is terminated by a phase-matching layer of thickness d and a medium with complex refractive index $\underline{n}_m$. It can be shown that this combination can be treated as a different, lossless medium with an effective refractive index n_r at the Bragg-wavelength.

For $n_s = n_1$, there is a well-known easy formula for calculating the peak reflectivity at Bragg wavelength. As this is not the case for this structure, we have to write

$$\underline{\rho} = \pm \frac{r(n_r + n_2) - (n_r - n_2)}{(n_r + n_2) - r(n_r - n_2)} \quad \text{with} \quad r = \pm \frac{\left(\frac{n_2}{n_1}\right)^{2N} - \frac{n_2}{n_S}}{\left(\frac{n_2}{n_1}\right)^{2N} + \frac{n_2}{n_S}}. \tag{2}$$

In (2), we choose "+" if the mirror configuration is like in Fig. 2 with N pairs. In case the last layer next to the medium (refractive index n_2) is missing, i.e., for $N - 1/2$ pairs, we choose "−." Now, we like to calculate a hybrid mirror as depicted in Fig. 2 with gold as complex refractive index material $\underline{n}_m = 0.43 - j8.5$. The corresponding amplitude reflection factor $\underline{\rho} = -0.932 + j0.315$ for an observer medium $n_1 = 1.4$ can be easily found, yielding $R = 96.8\%$. This complex reflectivity factor can be made real by inserting a phase matching layer of thickness d, as depicted in Fig. 2, with

$$d = \frac{\lambda}{4n_1}\left(1 + \frac{1}{\pi}\arctan\left(\frac{\text{Im}(\underline{\rho})}{\text{Re}(\underline{\rho})}\right)\right) = \frac{\lambda}{4n_1}\left(1 - \frac{1}{\pi}\arctan\left(\frac{2n_1\kappa}{n^2 + \kappa^2 - n_1^2}\right)\right) \tag{3}$$

assuming $\underline{n}_m = n - j\kappa$. For the upper case, d would become 89.6% of a quarter wavelength. The effective reflection factor becomes $\rho_r = \sqrt{R}$, and the corresponding effective refractive index n_r at Bragg wavelength against an observer medium n_1 would be $n_r = 0.01133$. The total reflectivity of the hybrid mirror like in Fig. 2 can therefore also be evaluated by (2). For the current VCSEL-structure with 3.5 mirror-pairs $(n_1 = 1.4, n_2 = 2.3, n_s = 3.2)$ and gold termination, i.e., three mirror pairs and effective refractive index terminating media n_r as calculated above, we find a reflectivity $\rho = 99.96\%$ $(R = 99.93\%)$. With these extremely high reflectivities, this kind of mirror is especially qualified as a bottom-mirror of a VCSEL, where no light is coupled out.

2.2. BTJ

There are several reasons why no reasonable performing long-wavelength VCSELs could be presented up to now without incorporating a tunnel junction. The main reason is that p-conducting semiconductor material is especially lossy for longer wavelength, as free carrier absorption α_{fc} raises with the square of the wavelength λ and hole mobilities μ_h are much lower [13]

$$\alpha_{fc} = \frac{\lambda^2}{n}\frac{e^3}{4\pi^2\varepsilon_0 c^3}\left(\frac{N}{m_e^2\mu_e} + \frac{P}{m_h^2\mu_h}\right) \tag{4}$$

with n as the refractive index, electron and hole masses and mobilities m_e and m_h and μ_e and μ_h for conductivity, doping concentrations N and P, and the natural constants e, ε_0 and c. Together with

the thick mirrors of layers of low refractive index contrast, this translates into high cavity losses, low achievable mirror reflectivities, and, therefore, poor laser performance. A tunnel junction can convert hole current into electron current and therefore replace lossy *p*-conducting by favorable *n*-conducting semiconductor material. In a VCSEL structure with a standing cavity wave aligned with the epitaxial layers, one can place a thin tunnel junction into a node of the optical wave. Therefore, even using highly doped, low-bandgap *p*- and *n*-conducting materials with very high optical losses, the effective cavity losses can be negligible for a properly placed BTJ. Consequently, the total cavity losses can be lowered with this approach.

Second, with low hole mobilities, together with low doping levels avoiding extensive cavity losses as discussed above, high series resistances would be the consequence as the specific electrical conductivity σ of a semiconductor material is given as

$$\sigma = eE(\mu_e N + \mu_h P) \tag{5}$$

with E as the electrical field applied. This would mean high *RC*-products and extensive ohmic heating both drastically limiting the high-speed performance. Therefore, with a well-designed BTJ, very low ohmic devices can be realized, especially qualified for high-speed modulation.

Finally, forming current apertures by oxidation is not possible in the InP-based material system, as Indium effectively inhibits selective wet oxidation processes. Hence, other ways of forming a current aperture have to be found. In our case, the tunnel junction is structured by lithography, and the highly doped tunneling layer is etched away where no current is supposed to flow. This converts the ohmic tunnel junction into a blocking reverse-biased diode, forbidding current to flow on the outer region, forming an aperture for the VCSEL structure. Besides the necessity of a second epitaxial run, this is a very elegant way of forming apertures for VCSELs as the wet oxidation is a treacherous gift thinking about single-mode devices. The oxidation rate of AlGaAs exponentially depends on the aluminum content and oxidation temperature and further depends on the mesa size, speeding up at the end of the oxidation. Accordingly VCSEL apertures formed by wet oxidation are hard to control. This results in low yield thinking about single-mode devices. Therefore, technologies like the BTJ defining the aperture size by lithography are favored not only in the research environment.

The tunnel junction itself consists of highly doped low bandgap material, where nondiffusing dopants like carbon or silicon are preferred. Highly conductive and ohmic interfaces can be realized. Hetero-barriers for holes and electrons in the cladding layers should be avoided or overcome by graded interfaces toward the tunnel junction as otherwise, significant voltage drops can occur. To avoid losses, the BTJ layers should be as thin as possible. Also, thickness control is essential to guarantee the positioning of the BTJ versus the optical cavity wave.

To sum up, the BTJ concept [9] enabled room-temperature operation of long wavelength VCSELs with reasonable performance.

3. High-Speed Limitations

From rate equation analysis, the theoretical transfer function [see (1)] describing the modulation response of a laser can be found. Besides resonance frequency and parasitic, intrinsic damping limits, the modulation speed could be found. Further, damping and oscillation frequency are connected

$$\gamma = f_R^2 \cdot K + \gamma_0 \quad \text{and} \quad K = 4\pi^2 \tau_p \left(1 + \Gamma \frac{a_p}{a}\right) \tag{6}$$

with the K-factor mainly depending on the photon-lifetime τ_p. The damping offset γ_0 is caused by the spontaneous emission and would become worse for lasers with high threshold current. Further, K is influenced by the differential gain a, the negative gain derivate after photon density a_p, and the

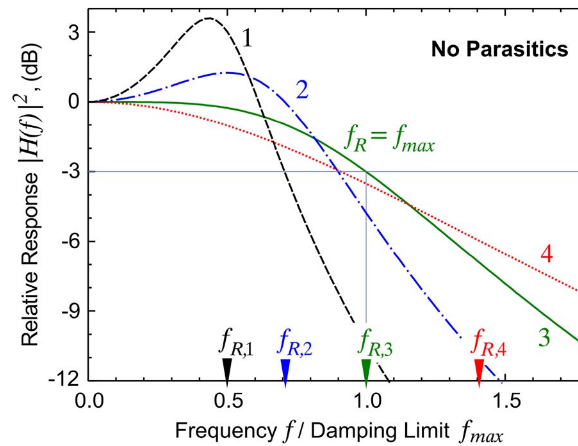

Fig. 3. Damping limited bandwidth. The small-signal response of an ideal laser diode is calculated for various oscillation frequencies $f_{R,n}$. For higher f_R, both damping and bandwidth increase up to the maximum bandwidth $f_{\max}$.

optical confinement factor Γ. This K-factor gives us a proportionality predicting when the system is going to be overdamped, yielding a maximum achievable bandwidth $f_{\max}$ of 2.83 π/K. Fig. 3 illustrates this mechanism, presenting calculated modulation bandwidths for an ideal laser source without parasitics. For an oscillation frequency of only 50% of $f_{\max}$, a clear oscillation overshoot can be observed. Above $f_{\max}$, the system becomes overdamped, resulting in smaller bandwidth for greater f_R decreasing down to $2\pi/K$ for very large values of f_R.

Please note that for real devices, often, the parasitic limitation f_P, maximum achievable oscillation frequency $f_{R,\max}$, and $f_{\max}$ could have quite similar values. Then, a value of $2\pi/K$ is more realistic for the laser bandwidth $f_{3\,\mathrm{dB}}$. For overdamped systems, however, f_P is the limiting factor. On the other hand, especially for small bias currents, the relaxation oscillation frequency f_R itself has a big impact on the system bandwidth. Neglecting damping and parasitics, the bandwidth of the laser would become 1.55 f_R; this is also known as thermal bandwidth limit for high-speed VCSELs, where the thermal rollover and differential gain saturation forbids a further increase in driving current and resonance frequency.

For damping-free $(K = 0)$ lasers with very high oscillation frequencies, parasitics are the main limit. These assumptions may not look practical for real laser devices. However, with optical injection locking (OIL), the relaxation frequency can be boosted even above 100 GHz [14], and damping can be overcome by high injected powers [15]. On the other hand, these assumptions also apply for lasers not optimized for high-speed performance with large parasitics. Then, the parasitic bandwidth limit can be up to 3.74 times larger than the bandwidth f_P of the electrical parasitic network (assuming f_R to be tailored to be 3.19 f_P). This explains why with lasers designed for 10 Gb/s, up to 40 GHz bandwidth could be achieved under OIL [16]. For arbitrary resonance-frequencies and negligible damping, the achievable bandwidth over resonance frequency is plotted in Fig. 4, finding a quite linear interrelationship between the resonance frequency and the modulation bandwidth for $f_P < f_R < 3.19 f_P$.

However, for high-speed VCSELs without OIL, damping is rather high. Furthermore, already at $\gamma = 28.4 f_P$, the condition for overdamping is reached, and the bandwidth is dominated by the electrical parasitic and becomes $f_{3\,\mathrm{dB}} = f_R = f_P$. Practically, for high-speed, long-wavelength VCSELs, a bandwidth around 10% above the parasitic rolloff is realistic. A detailed derivation of the above equations can be found in [17].

As the electrical parasitic turned out to be one crucial limiting factor, it was investigated in detail. In order to identify the limiting elements, we extracted parasitic responses from S_{11}-measurements and did equivalent circuit fitting, as presented in Fig. 5. The simple three-element circuit, as presented in the center of Fig. 5(a), is mathematically equivalent to curve fitting with (1) [17].

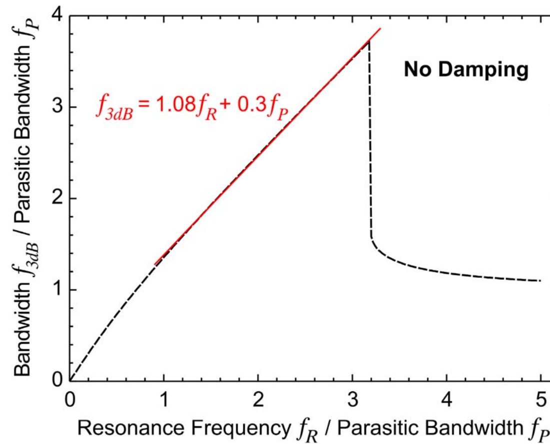

Fig. 4. Parasitic limited bandwidth without damping. Numerical solution of (1). With resonance-frequencies significantly higher than the parasitic roll-off, the modulation bandwidth can be extended. Curve fitting allows a quite easy approximate formula to be found.

Therefore, relaxation oscillation frequency f_R, damping rate γ, and the parasitic rolloff frequency f_p can be directly translated into equivalent circuit elements

$$f_R = \frac{1}{2\pi\sqrt{LC}}, \qquad \gamma = \frac{1}{RC}, \qquad f_p = \frac{R_m + R_a + Z_{50\,\Omega}}{2\pi(R_m + Z_{50\Omega})C_a R_a} \tag{7}$$

with $Z_{50\,\Omega}$ as impedance of the used RF-sources $(\text{usually} = 50\ \Omega)$. Equivalent circuit elements are as defined in Fig. 5(a). We achieved excellent curve fits with that method and, therefore, also expect good agreement for this case. The VCSELs under investigation, placed as neighbors on the same wafer, had an identical optical resonator but various semiconductor chip diameters. Biasing conditions were kept identical.

Generally, equivalent circuit modeling and their fits only represent a mathematical equivalent which do not necessarily need to represent physical equivalents. Therefore, mapping of those element values to physical device properties should be done carefully by verifying with other investigation methods like evaluating static differential series resistances, sample structures, and comparison between different structures as well. Especially rather complicated equivalent circuits tend to have many mathematical solutions which do not necessarily have a physical correspondence. On the other hand, fitting circuits to measured device properties is a nontrivial problem. Only for very simple circuits, e.g., like the one used here, comprising only three elements, curve fitting can be done on an equation basis. For four elements, equations become rather bulky, requiring vast computing times while fitting, and already for five elements, the equations can no longer be inserted in common curve-fitting software tools. Therefore, equivalent circuit fitting is usually being done using very powerful and specialized design simulation software.

In Fig. 5, we present an equivalent circuit analysis done for two different parasitic circuit models. In (a), we show our simple three-element circuit EC (1) associated with device layout, and in (b), a more sophisticated EC (2) comprising five lumped elements is given. The active region is modeled according (1) and translated into an *RLC* circuit, which is also presented here. The step from EC (1) to EC (2) was motivated as resistances and capacitances in the laser chip are spread. Consequently, a two-stage approach, dividing resistors and capacitances, should model the device even more precisely. Accordingly, the device impedance, as presented in Fig. 5(c) and (d), is fit, especially for small bias currents, with higher accuracy in (d), utilizing EC (2). The extracted element values via the biasing conditions of the VCSEL are presented in Fig. 5(e) and (f) for EC (1) and (2), respectively.

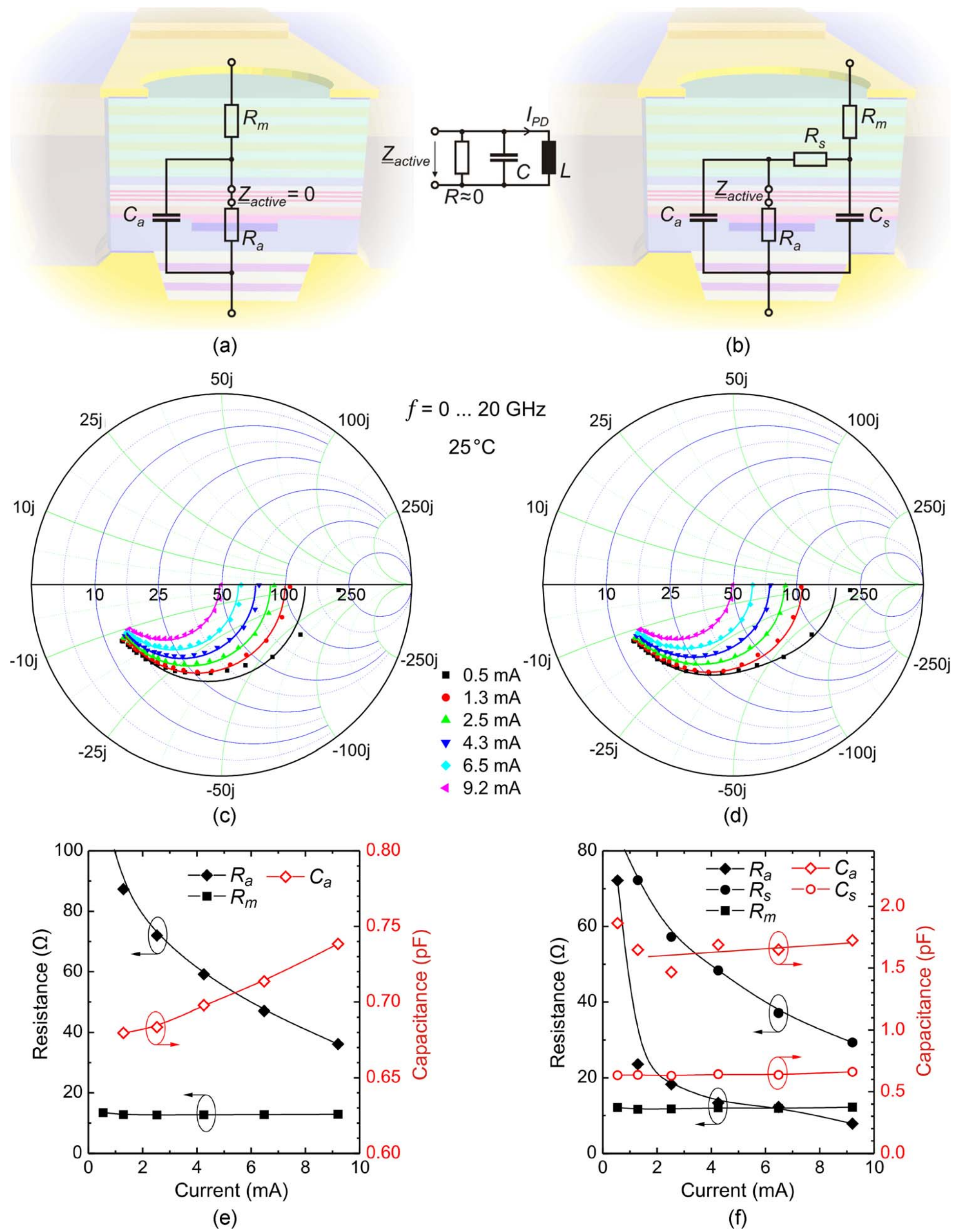

Fig. 5. Equivalent circuit (EC) analysis done for a 1.55-μm BTJ VCSEL: 28-μm chip diameter, 4-μm aperture diameter, high-doping overgrowth, BCB design, various bias currents. (a) Simple EC (1) and (b) Refined EC (2). The damped second-order transfer-function of the active region can be modeled by an *RLC* circuit, as depicted. In (c), VCSEL S_{11} fit to EC (1), and in (d), VCSEL S_{11} fit to EC (2). (e) and (b) Element values for EC (1), respectively, EC (2).

After device value extraction, the parasitic pole f_P can be calculated via (7). Having access to all structure and design parameters, these EC investigations deliver very useful hints for device optimization. Fig. 6 shows the simulated influence of the parasitic capacitance C_a on the modulation bandwidth utilizing EC (1), predicting a large improvement potential. Consequently, we altered our VCSEL design introducing a 340-nm-thick layer of reduced doping down to $1.0 \cdot 10^{17}$ cm^{-3} in the overgrowth, expanding the space charge region and consequently reducing the space charge capacitance. At the same time, we could expect the series resistance R_m to rise. However, as can be seen in (7), R_m has no direct influence on f_P like C_a.

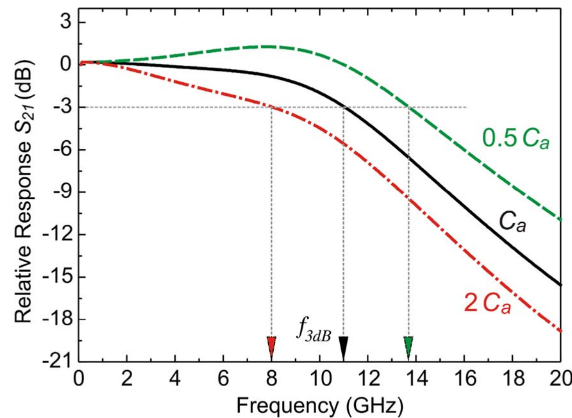

Fig. 6. Small-signal modulation performance 1.55 μm of the VCSEL presented in Fig. 5 at 6.5 mA bias current with virtually modified parasitic device capacitance C_a in EC (1) from Fig. 5(a). The drawn-through line represents the measured response; the green dashed line corresponds to the performance which would be expected for a C_a with half of its real value. The dash-dotted red line is for doubled C_a.

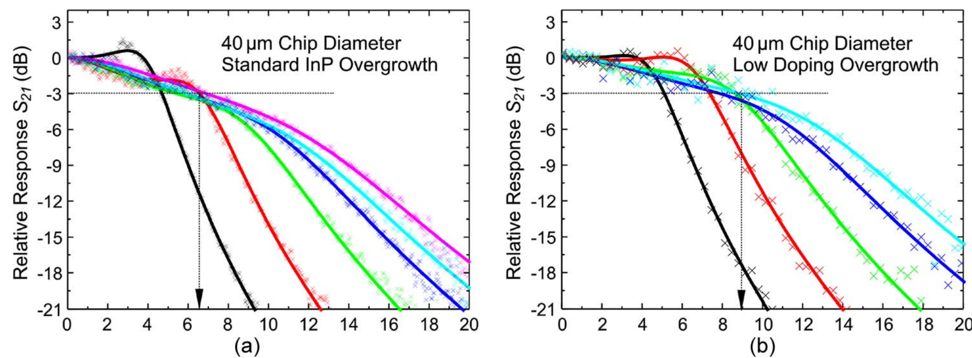

Fig. 7. Small-signal modulation performance of VCSELs with large chip sizes of 40 μm in diameter with varied design of the InP overgrowth. The solid lines present the excellent curve fits according to (1). As predicted in Fig. 6, a reduction in parasitic capacitance can drastically improve the transmission performance. (a) VCSEL with standard overgrowth, 5-μm aperture and 40-μm chip diameter causing a parasitically limited bandwidth of some 6.5 GHz. (b) Comparable VCSEL with improved overgrowth design as shown in Fig. 1 with reduced doping to lower the parasitic capacitance. A significantly enhanced bandwidth of 9 GHz can be stated. Smaller devices show even better performance.

The result is presented in Fig. 7. For a device with a rather large chip diameter of 40 μm, which used to be obviously limited by parasitic, the modulation bandwidth could be drastically improved from some 6.5 to 9 GHz. Smaller devices show even better performance.

Here, we intentionally present devices clearly limited by parasitic to underline the progress. Smaller devices are again limited by other effects like damping and thermal limitations, as discussed before.

4. High-Speed VCSEL Performance

These investigations led to an optimized VCSEL design with superior modulation capabilities. VCSELs are characterized by very high carrier and photon densities in the optical resonator, causing a damped modulation response. Consequently, low parasitics are especially important for VCSELs as the smaller relaxation oscillation overshoot cannot compensate a parasitic rolloff. Consequently, the intrinsic parasitic was drastically reduced, as discussed before. VCSELs as described in Section 2 were fabricated. The mode-gain offset was tailored to achieve temperature-invariant

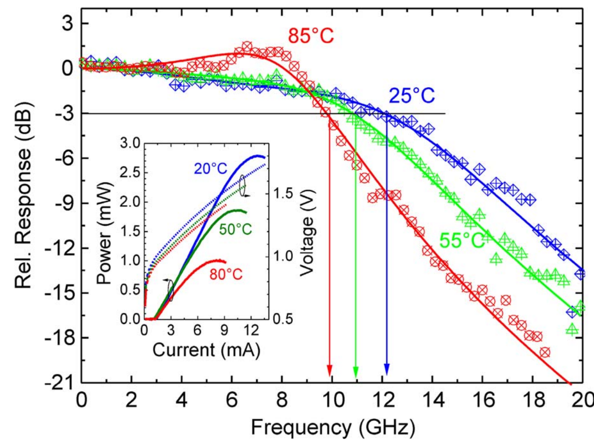

Fig. 8. Small-signal modulation performance of 1.55-μm VCSEL with improved modulation bandwidth and temperature range. At 25 °C modulation, bandwidth in excess of 12 GHz can be stated, and even at elevated temperatures of 85 °C, 10-GHz modulation bandwidth is available. Scatters: measured data; solid lines: fit to (1). *LIV*-characteristics given as inset.

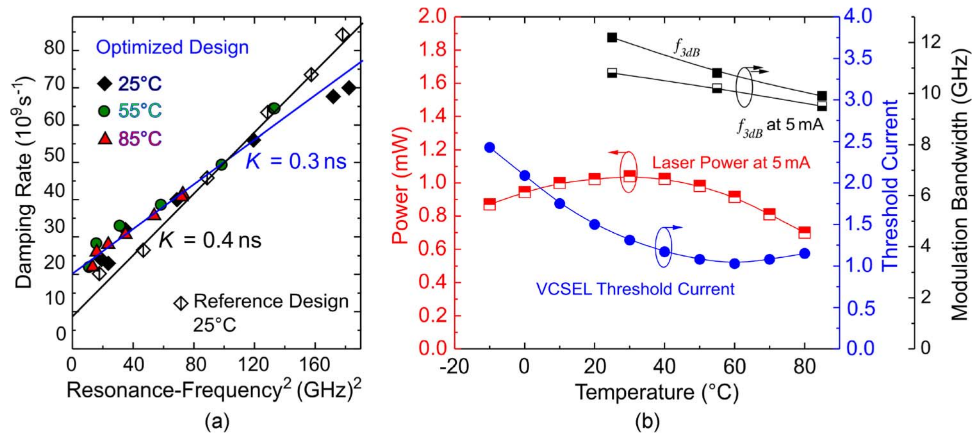

Fig. 9. Derived *K*-factor of new design compared with the reference design (a). Low damping and high bandwidth are achieved by a reduced *K*-factor and moderate damping offsets for all relevant operation temperatures. In (b), we present temperature behavior of VCSEL output-power, threshold current, and modulation bandwidth. For this VCSEL device, power and bandwidth are practically constant at 5 mA driving current over a wide temperature range, redundantizing monitor diodes.

device performance. The active region was designed for highest differential gain. Therefore, lower damping, better thermal properties, and a boosted modulation response due to reduced device parasitic were expected.

4.1. Modulation Performance

In Fig. 8, a superior modulation performance can be identified over a wide temperature range. The 3-dB bandwidth exceeds 12 GHz at 25 °C, is 11 GHz at 55 °C, and is 10 GHz at 85 °C. The *LIV*-performance is given as an inset showing more than 2.5 mW at room temperature and 1 mW at 80 °C. Fig. 9(a) plots the intrinsic damping γ derived from curve fitting to (1) versus the resonance-frequency squared deriving a temperature-invariant *K*-factor of 0.3 ns. The previous BTJ VCSEL generation had *K*-factors of 0.4 or more at room temperature, thus yielding an improvement of the damping limit. Further, the damping does not change with temperature; just the maximum driving current is limited by higher temperatures. This can also be observed in Fig. 8, where the red curve for

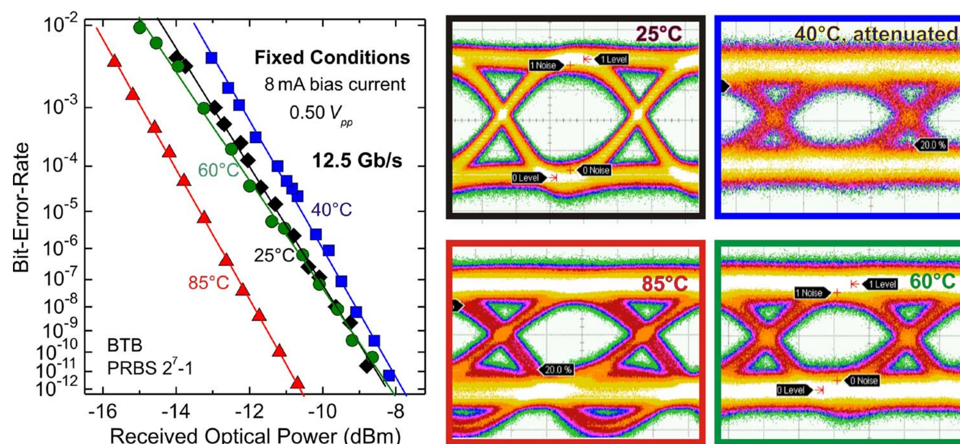

Fig. 10. Large-signal modulation performance of a VCSEL as presented in Fig. 1. Error-free data-transmission at 12.5 Gb/s data-rate up 85 °C with fixed biasing conditions is demonstrated. ($2^7 - 1$ PRBS, BTB, decision level optimized for 85 °C). Corresponding eye diagrams are also given.

85 °C heat-sink temperature has a clear relaxation overshoot, whereas the best curve for room temperature (blue) at higher driving currents is already overdamped.

In Fig. 9(b), several device-parameters are plotted versus temperature. The lowest threshold current can be found at 60 °C. This translates to almost constant power and constant bandwidth behavior for a given driving current.

For this kind of device, no temperature control, power monitoring, or fancy driving schemes, where the driver has to adjust the laser to environmental conditions, are needed. This is a very interesting design feature for these kinds of VCSELs, which can reduce the system cost significantly.

4.2. Large-Signal Data Transmission

Large-signal data transmission experiments are essential to judge the performance in digital data systems, since the measured laser bandwidth from small-signal experiments does not directly translate to such system performance. Performance of our VCSELs would be greatly under-estimated by common rules of thumb.

The VCSELs presented here were especially designed for uncooled operation with superior and constant rating. As demonstrated in Fig. 10, error-free data transmission at 12.5-Gb/s up to 85 °C is feasible without cooling or adjusting the driving conditions of the laser to the environment temperature. The receiver powers were limited by the low-sensitivity 12.5-GHz photo-detector and not the laser diode in that experiment. No erbium-doped fiber amplifier (EDFA) was used in that setup. Under fixed driving conditions and widely varied operation temperature, error-free data transmission could be achieved [7]. The corresponding 12.5-Gb/s eye diagrams are also depicted in Fig. 10.

In order to measure high data rates in excess of 25 Gb/s, we used a high-bandwidth photo-detector with the signal preamplified by an EDFA for better adjustment of decision levels on our bit-error-rate (BER) test equipment. Fiber coupling was stabilized actively. To test the polarization stability under modulation, we used a special polarization-maintaining EDFA. Consequently, a polarization flip would interrupt the error-free data stream. Received powers given are before the amplification by the EDFA and are still not limited by the laser. In Fig. 11(a), we present error-free data transmission at 25 Gb/s (BTB, $2^7 - 1$ PRBS, room temperature, 9.5 mA bias current, $0.7 V_{pp}$ modulation amplitude). The BER penalty as compared with 20 Gb/s transmission rate is 2.3 dB at a BER of 10^{-9}. Corresponding open-eye diagrams are presented in Fig. 11(b). Clear open eyes are demonstrated for data rates up to 25 Gb/s. With this laser, a 20-Gb/s data transmission over 6.5 km of SMF has also been reported recently [18].

Sometimes the question arises as to how a 12-GHz device can do error-free data transmission at 25 Gb/s with wide open eyes. For edge-emitting lasers, often, a higher bandwidth than the

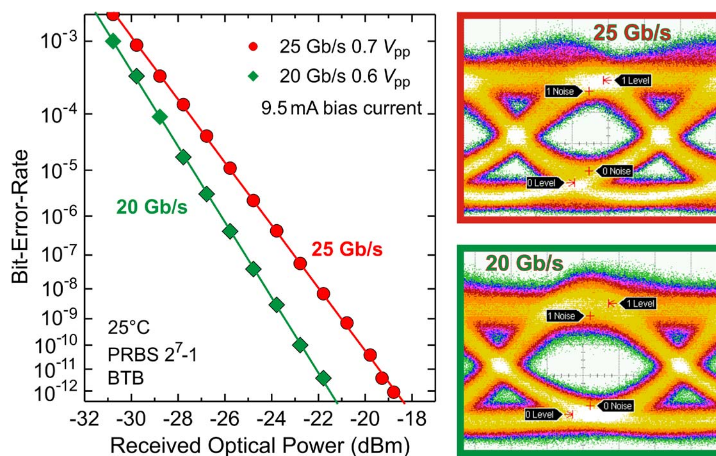

Fig. 11. Error-free data-transmission of a 1.55-μm high-speed VCSEL at 20 Gb/s and 25 Gb/s recorded at 25 °C and $2^7 - 1$ PRBS and corresponding wide-open eye diagrams.

achievable data rate is needed. These long-wavelength VCSELs are still mostly thermally limited. Therefore, on the one hand, the modulation response is overdamped and has a smooth shape without Bessel filtering. This favorable shape of the S_{21}-curve would enable 25 Gb/s in a nonreturn-to-zero (NRZ) modulation scheme at a bandwidth of only 70% of 25 GHz, i.e., 17 GHz, but there is another factor helping these lasers. The best large-signal modulation performance is carried out by biasing the lasers around or even above the CW thermal rollover. Driving these devices pulsed with a 50% duty cycle, the thermal rollover occurs much later, explaining this phenomena. Therefore, one would have to measure a 50% duty cycle S_{21}-curve for realistic comparison, which is not supported by our setup. The only tradeoff is that for very long coding schemes, with low frequencies interacting with long thermal time constants, and certain biasing conditions an error-floor could be observed. However, this would only affect long-haul networks, where neither VCSELs nor directly modulated lasers are applied. For cost-effective access networks, these devices have ideal properties.

For application schemes, these device properties enable, on the one hand, cost-effective top performance like 100G Ethernet with 4 $\times$ 25 Gb/s-VCSELs cooled for optimal performance. On the other hand, very attractive data rates of 10–14 Gb/s can be accommodated uncooled, with fixed driving conditions and without device monitoring, making really cost-effective solutions feasible.

5. Further Design Improvement

For future ultrahigh bit-rate communications applications like 100G Ethernet, optical interconnects, active cables, etc. higher bandwidths are needed at the long-wavelength side. Therefore, novel high-speed VCSELs with further improved modulation performance should be designed, manufactured, and characterized. Modulation bandwidths in excess of 20 GHz are expected, targeting at 25–40 Gb/s.

In order to realize even higher modulation speeds, the internal damping of the VCSEL cavity needs to be reduced. As the K-factor, characterizing the damping, mostly depends on the photon lifetime, a shorter optical resonator with shorter photon lifetimes is favorable. This could be realized in a novel high-speed VCSEL structure comprising two dielectric mirrors, as presented in Fig. 12.

As these dielectric mirrors feature a higher index contrast and, therefore, much lower penetration depths, the effective cavity length could be reduced drastically. Furthermore, in the novel design, the heat generated in the active region could also escape via the top current spreader consisting of InP, i.e., a good thermal conductor, which is connected to the golden large-area contact pad. A VCSEL with this structure was realized recently, yielding the expected improvements [8].

Moreover, the application of high-contrast gratings is a very effective way to maintain polarization mode stability in VCSEL devices. Besides that, they also have the potential to deliver higher single-mode output powers and improve back-reflection sensitivity as they preferably reflect

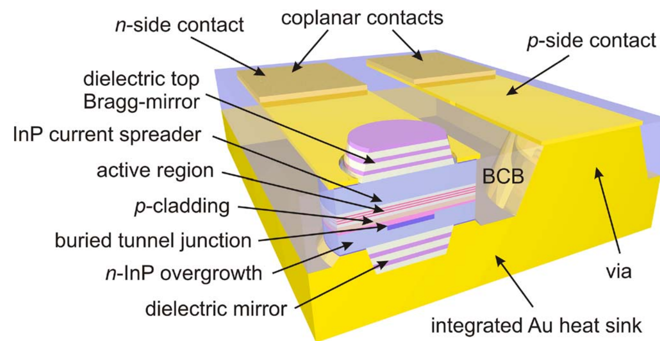

Fig. 12. Schematic cross-sectional image of a novel high-speed VCSEL structure with shorter cavity length. The epitaxial top-mirror with large penetration depths is replaced by a dielectric mirror with high index contrast. This design should feature lower photon life-times and, therefore, lower damping in the intrinsic response, enabling even higher modulation bandwidths.

the fundamental mode of the laser in one polarization direction. Single-mode, large-aperture devices have a smaller far-field angle, enabling efficient fiber coupling. Further, they show lower series resistances, reducing device parasitic. Providing certain power levels at high operation temperatures becomes easier with more active material, as Auger-recombination and thermal back-filling limits efficiency for long-wavelength devices based on low-bandgap materials. Therefore, a nanophotonic reflector is a very attractive candidate to replace the dielectric out-coupling mirror of the device in Fig. 11. This kind of device has also been realized very recently [19].

6. Conclusion

In this paper, we give an overview about our recent development of 1.55-μm BTJ VCSELs with improved high-speed and high-temperature performance. We explain proprietary design concepts and give a detailed description of our approach to achieve cutting-edge device performance. Internal parasitics have been drastically reduced by the redesign of doping levels. Modulation bandwidth at 5 mA is sufficient for 12.5 Gb/s over a temperature range from 0 °C to 85 °C at output powers around 1 mW. 25-Gb/s error-free data transmission has been demonstrated. Internal relaxation oscillation frequencies could also be improved by higher differential material gain from highly strained quantum-wells. In the meantime, further device optimizations have been realized as described here. These devices can deliver cost-effective ultrahigh modulation speeds in excess of 25 Gb/s or deliver ultralow cost solutions for the 10 Gb/s regime.

Acknowledgment

The lasers described here were developed at the Walter Schottky Institute, Technical University of Munich, under supervision of Prof. M.-C. Amann. Characterization was done in collaboration with Prof. D. Bimberg at the Institute of Solid State Physics, Technical University of Berlin. The author would like to acknowledge coworkers M. Müller for continuing these works at the Walter Schottky Institute, A. Nadtochiy for the measurements in Berlin, and M. Ortsiefer (CTO Vertilas GmbH) for his support in wafer mapping and die handling. Last but not least, the author would like to acknowledge Prof. C. Chang-Hasnain for her dedicated mentorship at Berkeley.

References

[1] F. Koyama, "Recent advances of VCSEL photonics," *J. Lightw. Technol.*, vol. 24, no. 12, pp. 4502–4513, Dec. 2006.
[2] P. Westbergh, J. Gustavsson, Å. Haglund, M. Sköld, A. Joel, and A. Larsson, "High-speed, low-current-density 850 nm VCSELs," *IEEE J. Sel. Topics Quantum Electron.*, vol. 15, no. 3, pp. 694–703, May/Jun. 2009.
[3] A. Mutig, S. Blokhin, A. Nadtochiy, G. Fiol, J. Lott, V. Shchukin, N. Ledenstov, and D. Bimberg, "High-speed 850 nm oxide-confined VCSELs for DATACOM applications," *Proc. SPIE*, vol. 7615, p. 76150N, 2010.

[4] N. Nishiyama, C. Caneau, B. Hall, G. Guryanov, M. H. Hu, X. S. Liu, M.-J. Li, R. Bhat, and C. E. Zah, "Long-wavelength vertical-cavity surface-emitting lasers on InP with lattice matched AlGaInAs–InP DBR grown by MOCVD," *IEEE J. Sel. Topics Quantum Electron.*, vol. 11, no. 5, pp. 990–998, Sep./Oct. 2005.

[5] A. Mereuta, G. Suruceanu, A. Caliman, V. Iacovlev, A. Sirbu, and E. Kapon, "10-Gb/s and 10-km error-free transmission up to 100 °C with 1.3-μm wavelength wafer-fused VCSELs," *Opt. Express*, vol. 17, no. 15, pp. 12 981–12 986, Jul. 2009.

[6] M.-C. Amann and W. Hofmann, "InP-based long-wavelength VCSELs and VCSEL arrays," *IEEE J. Sel. Topics Quantum Electron.*, vol. 15, no. 3, pp. 861–868, May/Jun. 2009.

[7] W. Hofmann, M. Müller, A. Nadtochiy, C. Meltzer, A. Mutig, G. Böhm, J. Rosskopf, D. Bimberg, M.-C. Amann, and C. Chang-Hasnain, "22-Gb/s long wavelength VCSELs," *Opt. Express*, vol. 17, no. 20, pp. 17547–17554, Sep. 2009.

[8] M. Müller, W. Hofmann, G. Böhm, and M.-C. Amann, "Short-cavity long-wavelength VCSELs with modulation bandwidths in excess of 15 GHz," *IEEE Photon. Technol. Lett.*, vol. 21, no. 21, pp. 1615–1617, Nov. 2009.

[9] M. Ortsiefer, R. Shau, G. Böhm, F. Köhler, and M.-C. Amann, "Low-threshold index-guided 1.5 μm long-wavelength vertical-cavity surface-emitting laser with high efficiency," *Appl. Phys. Lett.*, vol. 76, no. 16, pp. 2179–2181, Apr. 2000.

[10] W. Yuen, G. Li, R. Nabiev, J. Boucart, P. Kner, R. Stone, D. Zhang, M. Beaudoin, T. Zheng, C. He, M. Jensen, D. Worland, and C. Chang-Hasnain, "High-performance 1.6 μm single-epitaxy top-emitting VCSEL," *Electron. Lett.*, vol. 36, no. 13, pp. 1121–1123, Jun. 2000.

[11] W. Hofmann, M. Müller, G. Böhm, M. Ortsiefer, and M.-C. Amann, "1.55-μm VCSEL with enhanced modulation bandwidth and temperature range," *IEEE Photon. Technol. Lett.*, vol. 21, no. 13, pp. 923–925, Jul. 2009.

[12] S. Healy, P. O'Reilly, J. Gustavsson, P. Westbergh, Å. Haglund, A. Larsson, and A. Joel, "Active region design for high-speed 850-nm VCSELs," *IEEE J. Quantum Electron.*, vol. 46, no. 4, pp. 506–512, Apr. 2010.

[13] M.-C. Amann and J. Buus, *Tunable Laser Diodes*. Norwood, MA: Artech House, 1998.

[14] X. Zhao, E. Lau, D. Parekh, H.-K. Sung, W. Hofmann, M.-C. Amann, M. Wu, and C. Chang-Hasnain, "107-GHz resonance frequency of 1.55-μm VCSELs under ultra-high optical injection locking," in *Proc. CLEO/QELS*, San Jose, CA, 2008, pp. 1–2, CMW4.

[15] E. Lau, L. Wong, and M. Wu, "Enhanced modulation characteristics of optical injection-locked lasers: A tutorial," *IEEE J. Sel. Topics Quantum Electron.*, vol. 15, no. 3, pp. 618–633, May/Jun. 2009.

[16] L. Chrostowski, B. Faraji, W. Hofmann, M.-C. Amann, S. Wieczorek, and W. Chow, "40 GHz bandwidth and 64 GHz resonance frequency in injection-locked 1.55 μm VCSELs," *IEEE J. Sel. Topics Quantum Electron.*, vol. 13, no. 5, pp. 1200–1208, Sep./Oct. 2007.

[17] W. Hofmann, "InP-based long-wavelength VCSELs and VCSEL arrays for high-speed optical communication," in *Selected Topics of Semiconductor Physics and Technology*. Munich, Germany: Univ. Technol. Munich, 2009, pp. 25–40. [Online]. Available: http://nbn-resolving.de/urn/resolver.pl?urn:nbn:de:bvb:91-diss-20081119-679286-1-5

[18] L. Xu, W. Hofmann, H. Tsang, R. Penty, I. White, and M.-C. Amann, "1.55-μm VCSEL transmission performance up to 20 Gb/s for access networks," presented at the 14th Optoelectronics Communications Conf., Hong Kong, Jun. 2009, Post-Deadline Paper ThPD1-633.

[19] W. Hofmann, C. Chase, M. Mueller, Y. Rao, C. Grasse, M.-C. Amann, and C. Chang-Hasnain, "Long-wavelength high-contrast grating vertical-cavity surface-emitting laser," *IEEE Photon. J.*, vol. 2, no. 3, pp. 415–422, Jun. 2010.